Journal of Alloys and Compounds 509 (2011) 1607–1614

Contents lists available at ScienceDirect

Journal of Alloys and Compounds

journal homepage: www.elsevier.com/locate/jallcom

Electrical, magnetic, and Hall properties of $Al_xCoCrFeNi$ high-entropy alloys

Yih-Farn Kao[a], Swe-Kai Chen[b,c,*], Ting-Jie Chen[a], Po-Chou Chu[a], Jien-Wei Yeh[a,c], Su-Jien Lin[a,c]

[a] Department of Materials Science and Engineering, National Tsing Hua University, 101 Kuang Fu Road Sec. 2, Hsinchu 30013, Taiwan, ROC
[b] Center for Nanotechnology, Materials Science, and Microsystems (CNMM), National Tsing Hua University, 101 Kuang Fu Road Sec. 2, Hsinchu 30013, Taiwan, ROC
[c] High-entropy Alloys Lab., National Tsing Hua University, 101 Kuang Fu Road Sec. 2, Hsinchu 30013, Taiwan, ROC

ARTICLE INFO

Article history:
Received 4 October 2010
Received in revised form 25 October 2010
Accepted 28 October 2010
Available online 10 November 2010

Keywords:
Bulk $Al_xCoCrFeNi$ alloys
Cast
Homogenization
Plastic deformation
Melt-spinning
Electrical resistivity
Hall effect
Carrier density
Carrier mobility
Magnetic property
Kondo-like effect
Lattice defects

ABSTRACT

This investigation explores the electrical and magnetic properties of as-cast, -homogenized, and -deformed $Al_xCoCrFeNi$ (C-*x*, H-*x*, and D-*x*, respectively) alloys at various temperatures from 4.2 to 300 K. Experimental results reveal that carrier density of the alloys is of 10^{22-23} cm^{-3}. H-*x* has a carrier mobility of 0.40–2.61 $cm^2\,V^{-1}\,s^{-1}$. The residual electrical resistivity of the alloys varies from 100 to 220 μΩ cm. The temperature coefficient of resistivity (TCR) of H-2.00 is small (82.5 ppm/K). Therefore, defects in the lattice dominate electrical transportation. Some compositions exhibit Kondo-like behavior. At 300 K, H-0.50, H-1.25, and H-2.00 are ferromagnetic, while H-0.00, H-0.25, and H-0.75 are paramagnetic. Al and AlNi-rich phases reduce the ferromagnetism of single FCC and single BCC H-*x*, respectively. Spin glass behavior of some compositions is also observed. Alloys H-*x* are of the hole-like carrier type, and ferromagnetic H-*x* exhibits an anomalous Hall effect (AHE).

1. Introduction

The first study on high-entropy alloys (HEAs) was published in 1996 [1]. Today, research into HEAs addresses their mechanical, anticorrosion, hydrogen storage [2], and thermophysical [3] properties, among others. Relevant results demonstrate that HEAs have simple microstructures in the form of a solid solution of multiple elements [4–6], a favorable capacity to form nano-scale precipitates [5,7], high thermal stability [8], superior extensive or compressive properties [9], extremely high hardness [10], excellent anticorrosive properties [11,12], and special thermophysical and magnetic properties [3]. The crystallinity of HEAs is commonly simple, even though they are comprised more than five elements. The simple crystal lattices exhibit both the individual characteristics of their constituents and collective characteristics. For example, they exhibit the collective mechanical and thermal properties of a solid solution, but the anticorrosion performance of its individual constituent elements.

Understanding the physical properties, including electrical, magnetic, and thermal properties, of HEAs can help in understanding their lattice. The magnetic property of $CoCrCuFeNiTi_x$ alloys [13] has been studied. The FCC solid solutions that comprise in CoCrCuFeNi and $CoCrCuFeNiTi_{0.5}$ alloys exhibit typical paramagnetism, whereas $CoCrCuFeNiTi_{0.8}$ and CoCrCuFeNiTi alloys exhibit superparamagnetism, which is attributable to the embedding of nanoparticle assemblies in the amorphous phase with the addition of Ti. $Al_xCoCrFeNi$ alloys have been widely studied to elucidate their microstructural and mechanical [4], anticorrosive [11], and thermally expansive [3] properties. However, their electrical and magnetic properties are still not fully understood. This investigation, which extends another, [4], aims to study the electrical and magnetic properties of $Al_xCoCrFeNi$ alloys by measuring resistivity, magnetization, and the Hall effect. The values of the relevant parameters obtained using these three methods will be compared with each other, to provide insight into the physical properties of $Al_xCoCrFeNi$ alloys.

2. Experimental details

A total of 40–50 g of Al, Co, Cr, Fe, and Ni with purities of greater than 99.5% was used to prepare $Al_xCoCrFeNi$ ($0 \le x \le 2$) alloys using a vacuum arc-remelter. After the alloys were re-melted, they were turned over and the process was repeated at least three times to ensure that the alloys were completely mixed. As-cast alloys were

* Corresponding author at: Center for Nanotechnology, Materials Science, and Microsystems (CNMM), National Tsing Hua University, 101 Kuang Fu Road Sec. 2, Hsinchu 30013, Taiwan, ROC. Tel.: +886 3 574 2569; fax: +886 3 571 3113.
E-mail address: skchen@mx.nthu.edu.tw (S.-K. Chen).

0925-8388/$ – see front matter © 2010 Elsevier B.V. All rights reserved.
doi:10.1016/j.jallcom.2010.10.210

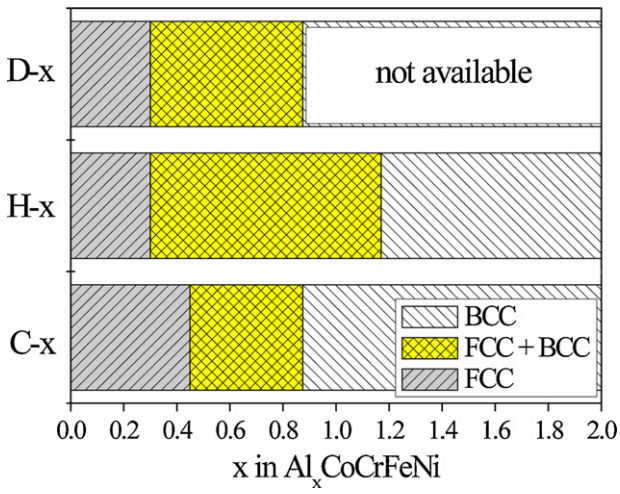

Fig. 1. Drawing for the x interval associated with phase boundary for alloys C-*x*, H-*x*, and D-*x*.

heated to 1100 °C at 20 °C per min and held at that temperature for 24 h. The samples were then quenched in water. These heated and quenched samples are called as-homogenized ones herein, except where otherwise specified. The as-homogenized samples were cold-deformed by a DBR250 two-high rolling mill to reduce their thickness by 75%. Cracks appeared in the samples with molar ratios of Al of more than 0.875 ($x > 0.875$) because they had high hardness. Therefore, the as-deformed samples were those with $0 \le x \le 0.875$ in this investigation. Here, C-*x*, H-*x*, and D-*x* represent as-cast, -homogenized, and -deformed $Al_xCoCrFeNi$ ($0 \le x \le 2$) alloys, respectively. Melt-spun samples with $x = 0.25$, M-0.25, were also prepared and their resistivity was measured and compared. The samples were cut using a diamond cutter into pieces with a thickness of 2 mm, and then ground to a thickness of less than 500 μm, using smaller-number sandpaper, to enable their resistivity to be measured. An EG & G Model 5210 Dual Phase Lock-in Amplifier was used to measure the resistance by the four-point probe method. To measure the resistivity of the samples at low temperatures, the samples were gradually sunk into liquid helium in a Dewar flask, and their resistance was continuously measured between 300 and 4.2 K. A superconducting quantum interference device magnetometer MPMS5 (SQUID), from American Quantum Design, was used to measure the magnetic properties of the samples, including the hysteresis loop (*M*–*H* curve) and the magnetization vs. temperature curve (*M*–*T* curve). The two states in which the *M*–*T* curves were measured were the zero-field cooling (ZFC) and field cooling (FC) ones. The hysteresis loops were measured at 300, 50, and 5 K. The *M*–*T* curves of 5–150 K were measured in a magnetic field of 100 Oe. The manipulating current that was used to measure the Hall effect was 10 mA; the applied magnetic field was up to ±9 T, and the temperature range was 5–300 K.

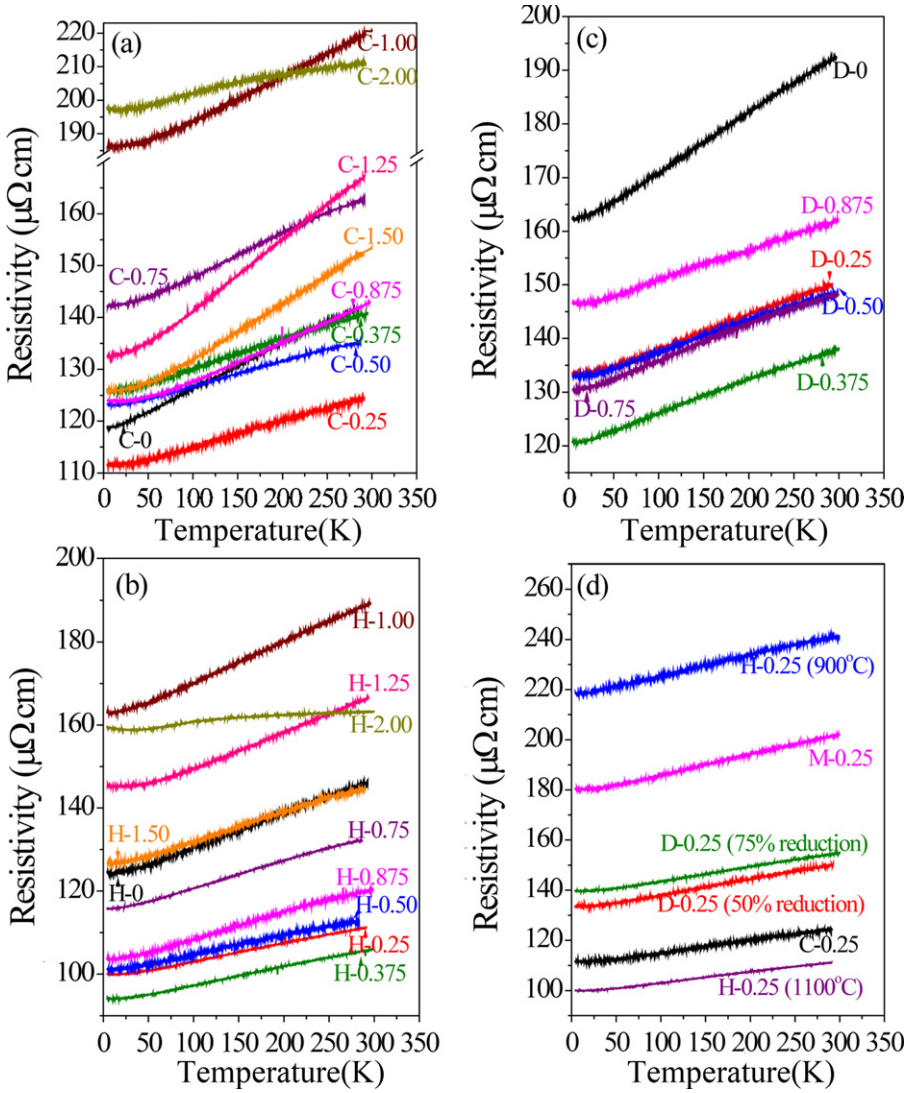

Fig. 2. (a) Experimental data of $\rho(T)$ for alloys C-*x*, (b) alloys H-*x*, and (c) alloys D-*x*, and (d) alloy $Al_{0.25}CoCrFeNi$ at various conditions.

3. Results and discussion

3.1. Microstructure of alloys C-x, H-x, D-x, 900 °C-homogenized H-0.25, and M-0.25

As shown in Fig. 1, the structures of the alloys C-*x*, H-*x*, and D-*x*, (with increasing amount of Al, given by *x*) are single FCC, duplex FCC–BCC, and single BCC, respectively. Al is a BCC stabilizer in $Al_xCoCrFeNi$ alloys. The ranges of *x* in which the alloys C-*x*, H-*x*, and D-*x* are in a duplex phase are $0.45 \le x \le 0.88$, $0.30 \le x \le 1.17$, and $0.30 \le x \le 0.875$, respectively [4]. Alloys 900 °C-homogenized-H-0.25 and M-0.25 comprise duplex FCC-AlNi-rich precipitate BCC and single FCC, respectively.

3.2. Electrical properties

3.2.1. Highly concentrated point defects in lattice of HEAs

Fig. 2(a)–(c) presents resistivity data for alloys C-*x*, H-*x* (*x* = 0–2.00), and D-*x*′ (*x*′ = 0–0.875), respectively, from 4.2 to 300 K. Table 1 lists the resistivity at 4.2 K (ρ_0), resistivity at 300 K (ρ_{300}), residual resistivity ratio (RRR), defined as ρ_0/ρ_{300}, and temperature coefficient of resistivity (TCR) defined as $(\rho_{300} - \rho_{150})/[\rho_{150}(300 - 150)]$.

Studies [4,14] have shown that Al is a strong BCC former and can promote atomic bonding in high-entropy alloys (HEAs). Therefore, the mechanical property [15], wear behavior [16], and anti-corrosion ability [17] are closely related to the Al content. However, no linear relationship between resistivity and *x* is observed in Fig. 2(a)–(c), indicating that the microstructure is not the only factor that affects the electrical resistivity of this alloy system. The ranges of the ρ_0 values of alloys C-*x*, H-*x*, and D-*x* are 111.06–196.49, 93.78–162.77, and 120.48–162.05 μΩ cm, respectively. The ρ_0 values of amorphous $AlCoCrCu_{0.5}FeNi$ [18] and Nd–Fe–B [19] alloys are 289 and 250 μΩ cm, respectively; the ρ_0 values of crystallized ternary $Ni_{75}Fe_{17}Cr_8$, $Ni_{75}Fe_{13}Cr_{12}$, and $Ni_{68}Fe_{17.5}Cr_{14.5}$ alloys are 58.1, 89.6, and 92.4 μΩ cm, respectively [20]. The ρ_0 values of the quinary alloys of interest herein exceed those of the aforementioned traditional crystalline alloys, but are less than those of amorphous alloys. Electron transportation is usually associated with the 'orderliness' of a lattice. The above discussion suggests that the orderliness of the lattices of the studied alloys is between that of an ordered structure (traditional crystalline alloys) and that of a disordered structure (amorphous alloy). HEAs exhibit long-range order but seemingly less degree short-range order in the sense of a single lattice. With respect to electronic conduction, quinary HEAs are metallic (see below)

Table 1
Electrical properties: ρ_0 (resistivity at 4.2 K), $\rho_{300\ K}$ (resistivity at 300 K), RRR (residual resistivity ratio), and TCR (temperature coefficient of resistivity) for alloys C-*x*, H-*x*, and D-*x*.

Alloys	ρ_0 (μΩ cm)	$\rho_{300\ K}$ (μΩ cm)	RRR	TCR (150–300 K) (ppm/K)
C-0	118.61	141.83	1.20	620
C-0.25	111.06	124.76	1.12	438
C-0.375	125.46	141.01	1.12	416
C-0.50	123.05	135.18	1.10	338
C-0.75	142.05	162.87	1.15	508
C-0.875	123.73	142.97	1.16	597
C-1.00	185.60	220.82	1.19	703
C-1.25	132.32	167.41	1.27	927
C-1.50	125.37	153.41	1.22	816
C-2.00	196.49	211.29	1.08	227
H-0	123.84	146.59	1.18	619
H-0.25	99.88	111.22	1.11	388
H-0.375	93.78	106.00	1.13	444
H-0.50	100.67	113.06	1.12	390
H-0.75	115.68	132.34	1.14	479
H-0.875	103.33	120.87	1.17	584
H-1.00	162.77	189.56	1.16	581
H-1.25	144.96	166.71	1.15	586
H-1.50	126.55	145.01	1.15	508
H-2.00	158.68	163.28	1.03	82.5
D-0	162.05	192.73	1.19	645
D-0.25	133.30	150.28	1.13	432
D-0.375	120.48	138.18	1.15	481
D-0.50	132.68	148.96	1.12	417
D-0.75	130.19	148.32	1.14	463
D-0.875	146.17	162.21	1.11	369

Table 2
Coefficients of fitted curves based on the formula $\rho = \rho_0 + A\ln(T) + BT^2 + CT^3$ for C-*x*, H-*x*, and D-*x* at low temperatures.

Alloys	Range of fit (K)	ρ_0 (μΩ cm)	A (10^{-2} μΩ cm)	B (10^{-5} μΩ cm K^{-2})	C (10^{-6} μΩ cm K^{-3})
C-0	4.2–20	118.71	–	75	60
C-0.25	8.4–33.6	111.60	−5.80	48	–
C-0.375	10.8–23.1	126.58	−44.41	166	–
C-0.50	7.4–29.4	123.62	−23.91	75	–
C-0.75	4.2–20	142.21	–	81	–
C-0.875	4.2–20	123.86	–	–	6.81
C-1.00	4.2–20	186.18	–	–	60
C-1.25	4.2–20	132.48	–	98	20
C-1.50	4.2–20	125.80	–	31	–
C-2.00	9.8–39.2	197.21	−3.25	35	–
H-0	4.2–20	124.19	–	46	20
H-0.25	6.3–24.9	100.08	−7.50	40	–
H-0.375	5.9–23.6	94.45	−19.93	77	–
H-0.50	4.8–19	101.91	−46.11	217	–
H-0.75	4.2–14.6	115.93	−13.47	136	–
H-0.875	4.2–16	104.40	−65.87	1365	–
H-1.00	5.3–21.1	163.31	−23.22	195	–
H-1.25	8.9–39.9	145.45	−8.80	5	5.86
H-1.50	5.4–21.8	127.34	−21.83	–	50
H-2.00	16.5–65.9	161.05	−76.06	36	0.17
D-0	4.2–20	162.21	–	185	–
D-0.25	4.2–20	133.56	–	–	20
D-0.375	4.4–17.8	121.17	−31.03	176	–
D-0.50	4.2–20	132.94	–	–	20
D-0.75	4.2–20	130.40	–	–	60
D-0.875	4.2–20	146.53	–	–	–

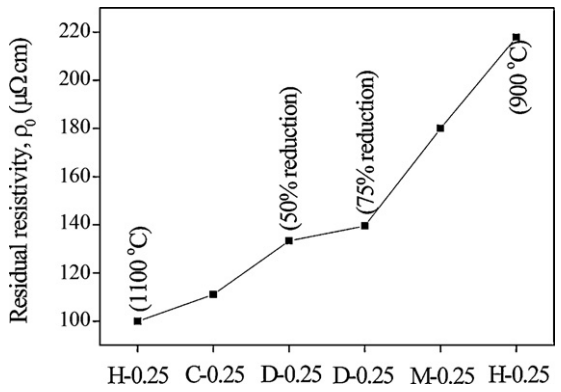

Fig. 3. Residual resistivity (ρ_0) for the alloy $Al_{0.25}$CoCrFeNi at as-cast, -homogenized (900 and 1100 °C), -cold-deformed (50% and 75% reduction in thickness), and -melt spun states.

but have highly-concentrated point defects, resulting from multi-principal elements in a pseudo-unitary lattice (PUL) cell. The RRR values range from 1.03 to 1.27, as indicated in Table 1. Accordingly, electronic transportation in the alloys of interest is dominated by the defects from 4.2 to 300 K, the defects in the lattice of alloys dominate electronic transportation therein. Additionally, the TCR value of H-*x* in Table 1 is low (82.5 ppm/K), because of the lesser orderliness of each lattice.

3.2.2. Resistivity of alloys FCC C-0.25, H-0.25, and D-0.25

Fig. 2(d) plots data on the resistivity of alloys C-0.25, H-0.25 (900 and 1100 °C), D-0.25 (50% and 75% reductions) and M-0.25 from 4.2 to 300 K. Fig. 3 reveals that the ρ_0 values increase in the order 1100 °C-homogenized H-0.25, C-0.25, 50% reduction-D-0.25, 75% reduction-D-0.25, M-0.25, and 900 °C-homogenized H-0.25. Greater deformation or a higher quenching/cooling rate corresponds to more introduced defects, and higher ρ_0 values. The 900 °C-homogenized H-0.25 has a relatively high ρ_0. This is associated with a small amount of BCC AlNi-rich precipitate [21]. Additionally, the ρ_0 of D-0.25 after 75% cold deformation slightly exceeds that of D-0.25 after 50% cold deformation.

3.2.3. Kondo-like behavior

The dependence of resistivity of temperature is not simple, because it usually involves several effects over several temperature ranges. Conduction electrons usually interact with phonons at high temperatures, such as 300–1000 K, and the dependence in this temperature range is $\rho \propto T$ [20,22,23]. Conduction electrons usually interact with magnetic atoms in the alloys at intermediate temperatures, such as 100–300 K, and $\rho \propto T^2$. When the temperature declines to 0–50 K, phonon (T^3), magnetic (T^2), and electron–electron interaction ($T^{1/2}$) effects occur simultaneously [20]. Hence, suitable temperature ranges must be carefully selected to study the influence of temperature on the effects of all of the above phenomena.

Experiments have shown two typical features of electrical conductivity at low temperatures. They are residual resistivity (equal to ρ_0, as described in Section 3.2.) and the Kondo effect [24]. Residual resistivity is the resistivity that is caused by the scattering of electron waves by static defects that disturb the periodicity of the lattice [22]. According to Matthiessen's rule, the net resistivity is given by $\rho = \rho_L + \rho_i$, where ρ_L represents the resistivity that is caused by the thermal phonons, and ρ_i is the residual resistivity. Therefore, $\rho_i(0)$ is the extrapolated resistivity to 0 K because ρ_L is commonly independent of the number of defects when the defect concentration is weak, and is usually proportional to the temperature. Therefore, ρ_L vanishes as T approaches 0 K. The Kondo effect, however, vanishes at high temperatures, but localized spin fluctuation and RKKY interaction [22] increase resistivity at low temperatures. The Kondo effect commonly arises in dilute alloy systems. Although HEAs are not dilute, they exhibit a Kondo-like behavior, which will be discussed in the following section.

Table 3
Coefficients of fitted curves based on the formula $\rho = \rho_0 + BT^2 + DT$ for C-*x*, H-*x*, and D-*x* at temperatures in the range of 100–300 K.

Alloys	Range of fit (K)	ρ_0 (μΩ cm)	B (10^{-5} μΩ cm K^{-2})	D (10^{-2} μΩ cm K^{-1})
C-0	120–300	117.98	–	8.48
	100–120	120.91	25	2.90
C-0.25	100–300	110.09	–	4.98
C-0.375	130–300	125.03	–	5.39
	100–130	126.27	15	2.29
C-0.50	150–300	122.70	–	4.42
	100–150	122.02	2	4.44
C-0.75	200–300	142.82	–	6.89
	100–200	139.24	0.87	8.39
C-0.875	200–300	119.45	–	7.86
	100–200	121.21	6	5.82
C-1.00	200–300	181.39	2	12.49
	100–200	180.72	3	12.53
C-1.25	150–300	128.10	–	13.45
	100–150	129.09	14	10.67
C-1.50	150–300	120.75	–	10.96
	100–150	122.40	10	8.48
C-2.00	180–300	200.24	–	3.71
	100–180	189.41	–	5.82
H-0	100–300	122.30	–	8.21
H-0.25	100–300	98.84	–	4.28
H-0.375	100–300	93.00	–	4.39
H-0.50	150–300	101.17	–	4.12
	100–150	100.21	3	4.16
H-0.75	150–300	115.27	–	6.01
	100–150	114.94	8	4.94
H-0.875	100–300	102.50	–	6.14
H-1.00	100–300	160.37	–	9.83
H-1.25	200–300	140.46	–	8.88
	100–200	141.04	3	8.07
H-1.50	100–300	125.29	–	6.83
H-2.00	180–300	160.72	–	0.85
	100–180	159.11	–	1.76
D-0	120–300	160.07	–	11.00
	100–120	159.63	–	11.16
D-0.25	100–300	131.80	–	6.31
D-0.375	150–300	120.76	–	5.80
	100–150	119.96	3	5.81
D-0.50	120–300	132.29	–	5.54
	100–120	132.44	15	3.43
D-0.75	130–300	130.40	–	6.08
	100–130	130.06	12	4.62
D-0.875	100–300	145.82	5.7	5.24

In Fig. 2(a)–(c), two formulae are applied to fit $\rho(T)$. At low temperatures (4.2–66 K), $\rho = \rho_0 + A\ln(T) + BT^2 + CT^3$ is used to model Kondo-like (A), magnetic (B), and low-temperature phonon (C) effects. At intermediate temperatures (100–300 K), the fitting formula, $\rho = \rho_0 + BT^2 + DT$, where B and D are the coefficients of magnetic and phonon effects, respectively, is utilized. The Kondo-like effect is usually considered [25] to be proportional to lnT at low temperatures, such that $\Delta\rho/\rho_{min} \propto \ln T$. Tables 2 and 3 display the results of fitting. Alloys C-*x* (*x* = 0.25–0.50, and 2.00), H-*x* (*x* = 0.25-2), and D-0.375 exhibit Kondo-like behavior. At low temperatures, B is clearly one to two orders of magnitude higher than at intermediate temperatures. A is always negative in Kondo-like samples, and larger absolute values of A are associated with a stronger Kondo-like effect, especially in H-2.00. The magnetic contribution, T^2, competes with the Kondo-like effect. When the magnetic contribution greatly exceeds the Kondo-like effect, resistivity remains constant with a change in temperature and levels off at low temperatures. The Kondo-like and the magnetic effects

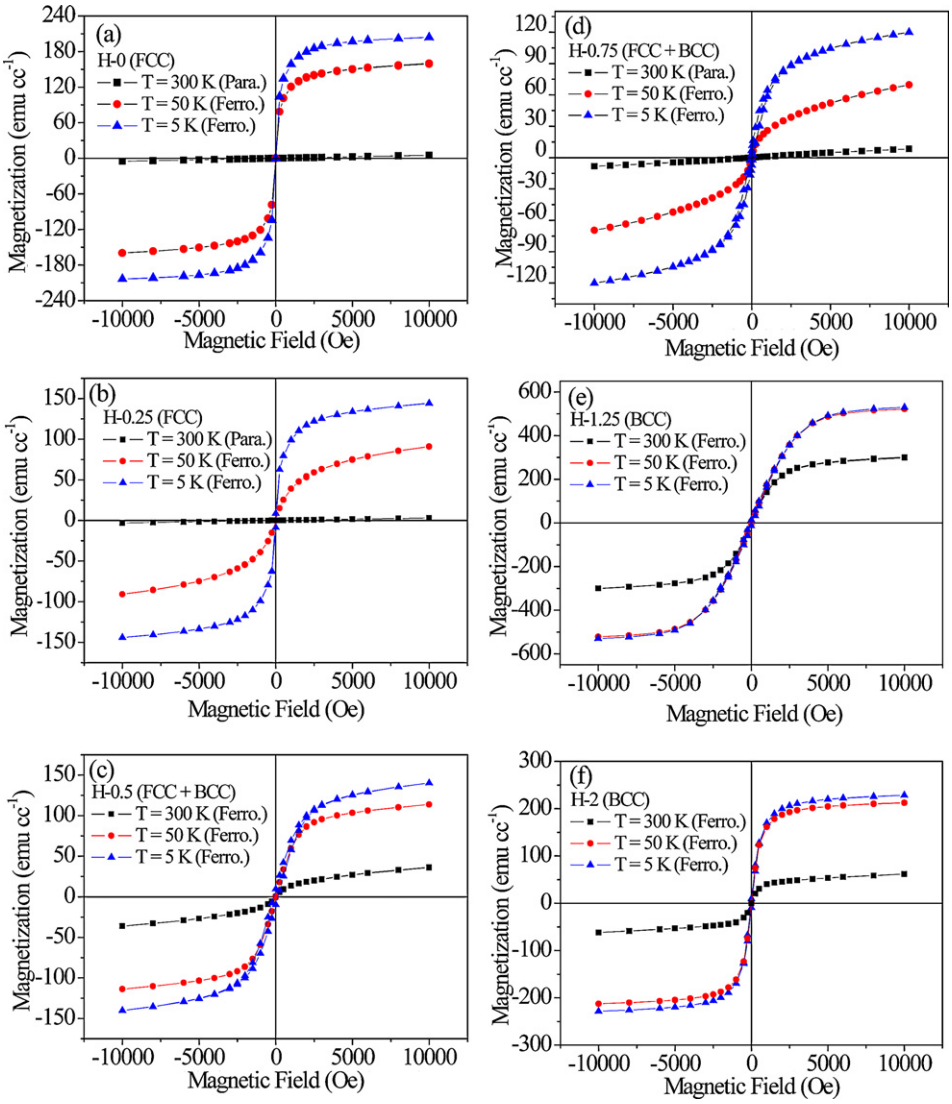

Fig. 4. Magnetization vs. magnetic field (M–H) curves from SQUID at 5, 50, and 300 K for (a) H-0, (b) H-0.25, (c) H-0.50, (d) H-0.75, (e) H-1.00, (f) H-1.25, and (g) H-2.00.

in H-x slightly increase with temperature at low temperatures, but the magnetic and phonon effects decrease with increasing temperature at intermediate temperatures. Evaluating the phonon effect at low temperatures, T^3, is difficult, because it is extremely small and frequently mixed with a magnetic effect, T^2 [20].

3.3. Magnetic properties of alloys H-x

Fig. 4(a)–(f) plot SQUID data for alloys H-x, respectively, at 5, 50, and 300 K. Table 4 presents the related magnetic parameters of alloys H-x. In the next two sections, most of the factors that are related to the magnetic property of alloys H-x, are associated with (i) the crystal structure and (ii) the Al or AlNi-rich phase.

First, the results that are explained by the crystal structure are discussed. Table 4 reveals that all H-x alloys are ferromagnetic at low temperatures (5 and 50 K). Additionally, the saturation magnetization (M_s) of alloys H-1.25 and H-2.00 exceeds that of alloys H-0 and H-0.25, indicating that at low temperatures, the BCC phase has a higher M_s value than the FCC phase. At room temperature (300 K), alloys H-0.50, H-1.25, and H-2.00 remain ferromagnetic, while alloys H-0, H-0.25, and H-0.75 are paramagnetic. The estimated Curie temperatures (T_C) are taken from the curves of the reciprocal of magnetic susceptibility (χ^{-1}) against temperature. Table 4 shows no regular relationship between T_C and x for alloys H-0, H-0.25, and H-0.50. Next, M_s, to which both BCC and FCC phases contribute, is estimated when $0.5 \le x \le 0.75$. The M_s of the two phases at 5 K can be calculated numerically as follows:

$$M_s = X_{FCC}M_{s,FCC} + X_{BCC}M_{s,BCC} \quad (1)$$

where X_{FCC}, $M_{s,FCC}$, X_{BCC}, and $M_{s,BCC}$ are the volume fraction of FCC, the saturation magnetization of FCC, the volume fraction of BCC, and the saturation magnetization of BCC, respectively. However, X_{FCC} and X_{BCC} can be obtained from the fitting of hardness [4]. Therefore, the above equation can be rewritten as,

$$140.11 = 0.7551M_{s,FCC} + 0.2449M_{s,BCC} \quad (\text{for H-0.50}) \quad (2)$$

$$119.93 = 0.5765M_{s,FCC} + 0.4235M_{s,BCC} \quad (\text{for H-0.75}) \quad (3)$$

Accordingly, $M_{s,FCC} = 167.78$ (emu cm^{-3}) and $M_{s,BCC} = 54.79$ (emu cm^{-3}). The reason for the result $M_{s,BCC} < M_{s,FCC}$ is ascribed to the existence of Al or AlNi-rich phase as discussed further in the following paragraph.

The results for which the Al or AlNi-rich phase are responsible is discussed. The M_s value declines as x increases in the ranges $0 \le x \le 0.25$ and $1.25 \le x \le 2.00$, as indicated in Table 4. The M_s and magnetic susceptibility (χ^{-1}) values of alloy H-0 are smaller than those of alloy H-0.25, implying that Al reduces the ferromagnetism

Table 4
A list of magnetic properties at 5 K, 50 K, and 300 K for alloys H-*x*.

Temperature	Parameters	H-0 (FCC)	H-0.25 (FCC)	H-0.50 (FCC + BCC)	H-0.75 (FCC + BCC)	H-1.25 (BCC)	H-2.00 (BCC)
5 K	State	Ferro.	Ferro.	Ferro.	Ferro.	Ferro.	Ferro.
	μ_H (μ_B)	0.25	0.18	0.17	0.15	0.67	0.29
	M_s (emu cm^{-3})	203.65	144.08	140.11	119.93	529.83	228.46
	M_r (emu cm^{-3})	0.94	8.54	9.48	6.90	13.87	9.53
	H_c (Oe)	2.24	30.08	137.95	71.31	76.46	30.92
	$S = M_r/M_s$[a], $\times 10^{-2}$	0.464	5.930	6.770	5.750	2.620	4.170
50 K	State	Ferro.	Ferro.	Ferro.	Ferro.	Ferro.	Ferro.
	μ_H (μ_B)	0.19	0.11	0.14	0.09	0.66	0.27
	M_s (emu cm^{-3})	159.14	90.84	113.80	69.60	521.73	212.22
	M_r (emu cm^{-3})	0.18	0.28	0.699	0.36	6.79	0.70
	H_c (Oe)	0.58	4.47	9.50	4.56	36.59	2.35
	$S = M_r/M_s$, $\times 10^{-2}$	0.113	0.308	0.614	0.517	1.300	0.330
300 K	State	Para.	Para.	Ferro.	Para.	Ferro.	Ferro.
	μ_H (μ_B)	–[b]	–	0.04	–	0.38	0.08
	χ (10^{-4} emu Oe^{-1} cm^{-3})	5.1	3.15	–	8.37	–	–
	M_s (emu cm^{-3})	–	–	36.36	–	301.35	61.79
	M_r (emu cm^{-3})	–	–	0.013	–	3.08	0.43
	H_c (Oe)	–	–	0.524	–	17.8	5.15
	$S = M_r/M_s$, $\times 10^{-2}$	–	–	0.036	–	1.020	0.696
	Estimated T_c (K)	120	90	335	200	440	375
	T_f[c] (K)	35	10	–	10	–	40

[a] "S" means squareness of the loop.
[b] "–" means not detectable.
[c] "T_f" is the temperature below which the magnetic state is spin glass in *M* vs. *T* curves measured in 5–150 K.

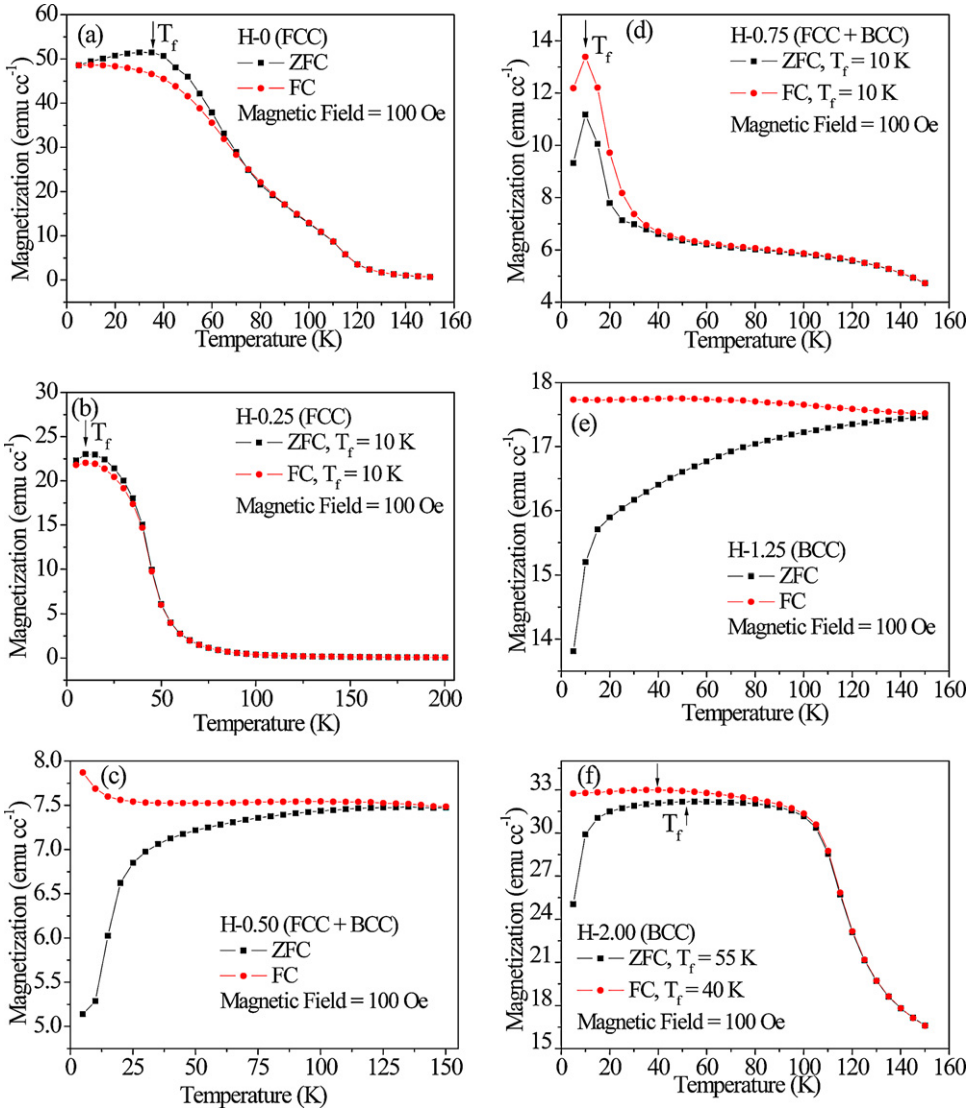

Fig. 5. Magnetization vs. temperature (*M*–*T*) curves under FC and ZFC conditions at 100 Oe for (a) H-0, (b) H-0.25, (c) H-0.50, (d) H-0.75, (e) H-1.00, (f) H-1.25, and (g) H-2.00.

Table 5
Parameters of Hall effect measurements at 9 T for H-*x*.

Parameters	Temperature (K)	H-0.25 (FCC)	H-0.50 (FCC + BCC)	H-0.75 (FCC + BCC)	H-1.00 (FCC + BCC)	H-1.25 (BCC)
Carrier type	–	Hole	Hole	Hole	Hole	Hole
Density (g cm^{-3})	–	7.92	7.80	7.58	7.10	6.83
Molecular weight	–	54.64	53.11	51.73	50.49	49.37
Carrier density[a] (10^{22} cm^{-3})	5	3.874	13.288	6.416	4.394	10.840
	300	5.767	8.298	3.339	2.718	1.436
Carrier mobility (cm^2 V^{-1} s^{-1})	5	1.61	0.46	0.84	0.87	0.40
	300	0.92	0.67	1.41	1.21	2.61
Valency	5	0.446	1.524	0.751	0.518	1.289
	300	0.664	0.963	0.391	0.321	0.171
Radius coefficient	5	3.46	2.30	2.93	3.32	2.46
	300	3.03	2.69	3.64	3.90	4.82
Fermi wave vector[b] (10^8 cm^{-1})	5	1.048	1.58	1.24	1.093	1.476
	300	1.196	1.351	0.997	0.931	0.753
Fermi velocity[c] (10^8 cm s^{-1})	5	1.212	1.828	1.434	1.264	1.708
	300	1.384	1.563	1.154	1.077	0.871
Fermi energy[d] (eV)	5	4.17	9.49	5.84	4.54	8.29
	300	5.44	6.94	3.78	3.30	2.15
Fermi temperature (10^4 K)	5	4.848	11.028	6.787	5.274	9.628
	300	6.322	8.057	4.391	3.828	2.502
Relaxation time (10^{-14} s)	5	0.078	0.024	0.042	0.043	0.020
	300	0.052	0.038	0.08	0.069	0.148
Mean free path (10^{-7} cm)	5	0.942	0.431	0.596	0.537	0.334
	300	0.723	0.590	0.922	0.739	1.284

[a] Carrier density is defined as N/V.
[b] $k_F = (3\pi^2 N/V)^{1/3}$.
[c] $v_F = (\hbar/m)(3\pi^2 N/V)^{1/3}$.
[d] $\varepsilon_F = \hbar^2 k_F^2/2m$.

of the FCC phase alloys ($0 \le x \le 0.25$). According to a study of Alnico magnets [26], the AlNi-rich phase exhibits weak ferromagnetism. In one study [4], H-2.00 contained an AlNi-rich ordered BCC phase. Hence, the fact that the M_s value of H-2.00 is smaller than that of H-1.25, which has no AlNi-rich ordered BCC phase, is unsurprising. In summary, Al reduces the ferromagnetism of single-FCC and single-BCC alloys H-*x*, by forming Al and AlNi-rich phases, respectively.

In Fig. 5(a)–(b) and (d)–(f), the maximum magnetization can be observed at 5–40 K. This reentrant spin glass behavior occurs at the freezing transition point (T_f) at which electronic spins are frozen.

3.4. Hall effect of alloys H-*x*

The Hall effect measurements are made in alloys H-0.25 (FCC), H-0.50 (duplex), H-0.75 (duplex), H-1.00 (duplex), and H-1.25 (BCC). Fig. 6(a)–(b) present data on the Hall resistivity (ρ_H) of the H-*x* samples at 5 and 300 K, respectively. Table 5 presents the related parameters.

Both the ordinary Hall effect (OHE) and the anomalous Hall effect (AHE) can be observed because of the ferromagnetism of the samples. Fig. 6 plots Hall resistivity (ρ_H) against magnetic field at 5 and 300 K, and reveals an obvious covariation of AHE and OHE. For alloys H-0.25 and H-0.75, at temperatures above the Curie temperature (300 K), only OHE occurs, while at temperatures below the Curie temperature (5 K), AHE clearly occurs. For H-1.25, the Curie temperature exceeds 300 K, and the curve at 300 K is shifted from that of 5 K since the magnetization is lower at 300 K. For AHE, the Hall resistivity ρ_H can be expressed as,

$$\rho_H = R_0 B + 4\pi M_s R_s \quad (4)$$

where R_0 is the ordinary Hall coefficient; B is the magnetic induction; M_s is the saturation magnetization, and R_s is the anomalous Hall coefficient. $R_0 B$ is the Lorentz force that acts on the conduction electrons, and the second term is attributable to the spin-orbit interaction [27–29] in a ferromagnet. The values of $R_s M_s$ and R_0 are obtained from the intercept and the slope, respectively, and the related fitting results are listed in Table 6. Notably, the M_s values of the samples are obtained from the SQUID data in Section 3.3. Only the ferromagnetic samples yield R_s values in Table 6, revealing that AHE dominates in ferromagnetic materials. Additionally, values of R_s at 5 K are close to those at 300 K, and this result shows that R_s is almost independent of temperature. Graphical analysis yields % of OHE and % of AHE, $\%_{OHE}$ and $\%_{AHE}$, can be obtained. The relevant equations are as follows:

$$\%_{OHE} = R_0 B/(R_0 B + 4\pi M_s R_s) \quad (5)$$

$$\%_{AHE} = 1 - \%_{OHE} \quad (6)$$

Table 6
R_0 (ordinary Hall coefficient), R_s (anomalous Hall coefficient), $\%_{OHE}$ (% of OHE), and $\%_{AHE}$ (% of AHE) at 5 K and 300 K for alloys H-*x*.

Alloys	5 K					300 K				
	R_0 (10^{-11} m^3 A^{-1} s^{-1})	R_sM_s (10^{-10} V m^2 A^{-2})	R_s (10^{-8} m^3 A^{-1} s^{-1})(%)	$\%_{OHE}$ (%)	$\%_{AHE}$ (%)	R_0 (10^{-11} m^3 A^{-1} s^{-1})	R_sM_s (10^{-10} V m^2 A^{-2})	R_s (10^{-8} m^3 A^{-1} s^{-1})	$\%_{OHE}$ (%)	$\%_{AHE}$ (%)
H-0.25	16.11	37.62	2.07	23.46	76.54	10.82	−1.15	–	100	0
H-0.50	4.70	26.28	1.49	11.35	88.65	7.52	−7.53	−1.64	NA[b]	NA[b]
H-0.75	9.73	37.23	2.46	15.77	84.23	18.70	9.23	–	100	0
H-1.00	14.21	80.05	NA[a]	11.28	88.72	22.97	−33.66	NA[a]	NA[b]	NA[b]
H-1.25	5.76	144.98	2.17	2.70	97.30	43.46	96.89	2.55	3.40	96.60

[a] "NA" means "not available", because H-1.00 is paramagnetic at both 5 K and 300 K.
[b] Calculation of R_s is omitted when R_sM_s is negative.

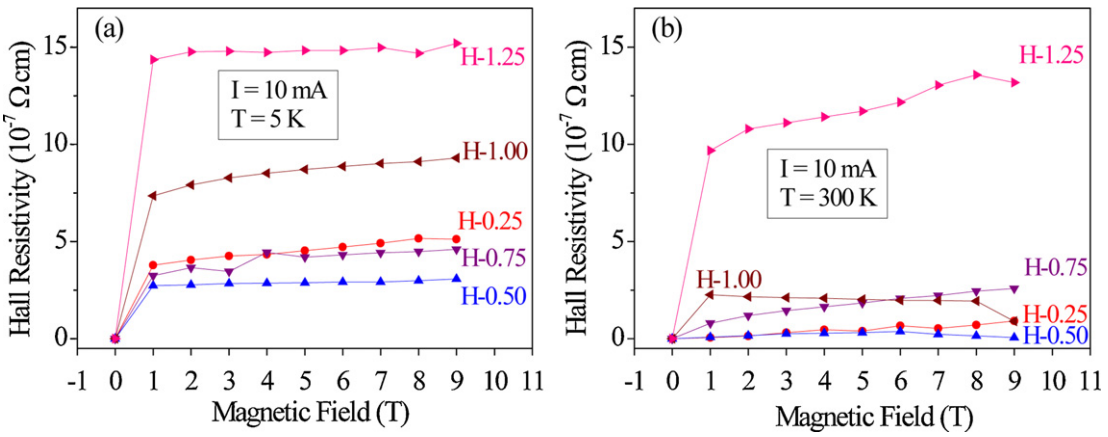

Fig. 6. Hall measurements using magnetic field 1–9 T for H-x (x = 0.25, 0.50, 0.75, 1.00, 1.25) at 5 K (a) and 300 K (b).

Table 6 presents $\%_{OHE}$ and $\%_{AHE}$ at 9 T. Clearly, $\%_{OHE}$ exceeds $\%_{AHE}$ at 300 K because H-x exhibits weaker ferromagnetism at 300 K than at 5 K. The $\%_{AHE}$ at 5 K is approximately equal to the saturation magnetization, M_S, at 5 K in Table 6. Samples with higher M_S, especially H-1.25, have higher $\%_{AHE}$, indicating that more strongly ferromagnetic samples have higher $\%_{AHE}$, and so $\%_{AHE}$ depends on the magnetism. The results in Fig. 6 support this conclusion.

The Hall resistivity of alloys H-x is positive, as shown in Fig. 6. These alloys are similar to Glassy TE-TL alloys [30]. The carriers in these samples are hole-like, although in some cases, the carriers are electron-like [31]. Based on ρ_H and ρ (the resistivity data in Section 3.2.), the related parameters of the Hall effect, presented in Table 5, can be obtained. The carrier density in a high-entropy alloy system H-x (10^{22-23} cm^{-3}) is similar to that in conventional alloys. However, the H-x high-entropy alloy system has lower carrier mobility (0.40–2.61 cm^2 V^{-1} s^{-1}) than conventional alloys with the same carrier density, because HEAs have heavier lattice defects than conventional alloys. This explanation warrants further study.

4. Conclusions

The values of ρ_0 at 4·2 K for alloys C-x, H-x, and D-x are 111.06–196.49, 93.78–162.77, and 120.48–162.05 μΩ cm, respectively. They are larger than those of conventional alloys with the same carrier density, but smaller than those of amorphous alloys. The RRR values range from 1.03 to 1.27. Therefore, the defects in the lattice dominate the electronic transportation in the studied alloy system. These facts imply that the density of defects in a single lattice in these high-entropy alloys is less than in amorphous alloys, but greater than in conventional alloys. The presented TCR value of H-2.00 is small (82.5 ppm/K). The fitted $\rho(T)$ reveals that some compositions exhibit Kondo-like behavior.

The single BCC structure in the alloy system has a high M_S value at low temperatures. At 300 K, alloys H-0.50, H-1.25, and H-2.00 are ferromagnetic, while alloys H-0.00, H-0.25, and H-0.75 are paramagnetic. Al and AlNi-rich phases reduce the ferromagnetism of single FCC and single BCC H-x alloys, respectively. Some of the compositions of interest in this investigation exhibit spin glass behavior.

Alloys H-x are of the hole-like carrier type. More strongly ferromagnetic alloys have higher $\%_{AHE}$, and an anomalous Hall effect (AHE) that depends more strongly on magnetism. The carrier density of H-x (10^{22-23} cm^{-3}) is similar to that of conventional alloys. Alloys H-x have a low carrier mobility (0.40–2.61 cm^2 V^{-1} s^{-1}), which is associated with the heavier lattice defects of HEAs than of the conventional alloys with the same carrier density.

Acknowledgement

SKC would like to thank the financial support of this research from the National Science Council of the Republic of China, Taiwan, under the Contract No. NSC96-2221-E007-066-MY3. Ted Knoy is appreciated for his editorial assistance.

References

[1] K.H. Huang, A Study on the Multicomponent Alloy Systems Containing Equal-mole Elements, M.S. thesis, Department of Material Science and Engineering, NTHU, Taiwan, 1996.
[2] Y.F. Kao, S.K. Chen, J.H. Sheu, J.T. Lin, W.E. Lin, J.W. Yeh, S.J. Lin, T.H. Liou, C.W. Wang, Int. J. Hydrogen Energy 35 (2010) 9046–9059.
[3] H.P. Chou, Y.S. Chang, S.K. Chen, J.W. Yeh, Mater. Sci. Eng. B163 (2009) 184–189.
[4] Y.F. Kao, T.J. Chen, S.K. Chen, J.W. Yeh, J. Alloys Compd. 52 (2009) 1026–1034.
[5] C.J. Tong, Y.L. Chen, S.K. Chen, J.W. Yeh, T.T. Shun, C.H. Tsai, S.J. Lin, S.Y. Chang, Metal. Mater. Trans. A36 (2005) 881–893.
[6] J.W. Yeh, Ann. Chim. Sci. Mater. 31 (2006) 633–648.
[7] J.W. Yeh, S.K. Chen, S.J. Lin, J.Y. Gan, T.S. Chin, T.T. Shun, C.H. Tsau, S.Y. Chang, Adv. Eng. Mater. 6 (2004) 299–303.
[8] S. Varalakshmi, M. Kamaraj, B.S. Murty, Mater. Sci. Eng. A527 (2010) 1027–1030.
[9] Y.J. Zhou, Y. Zhang, Y.L. Wang, G.L. Chen, Appl. Phys. Lett. 90 (2007) 181904–181906.
[10] K.C. Hsieh, C.F. Yu, W.T. Hsieh, W.R. Chiang, J.S. Ku, J.H. Lai, C.P. Tu, C.C. Yang, J. Alloys Compd. 483 (2009) 209–212.
[11] Y.F. Kao, T.D. Lee, S.K. Chen, Y.S. Chang, Corros. Sci. 52 (2010) 1026–1034.
[12] Y.Y. Chen, U.T. Hong, H.C. Shih, J.W. Yeh, T. Duval, Corros. Sci. 47 (2005) 2679–2699.
[13] X.F. Wang, Y. Zhang, Y. Qiao, G.L. Chen, Intermetallics 15 (2007) 357–362.
[14] W.Y. Tang, J.W. Yeh, Metall. Mater. Trans. A 40 (2009) 1479–1486.
[15] S.T. Chen, W.Y. Tang, Y.F. Kuo, S.Y. Chen, C.H. Tsau, T.T. Shun, J.W. Yeh, Mater. Sci. Eng. A 527 (2010) 5818–5825.
[16] J.M. Wu, S.J. Lin, J.W. Yeh, S.K. Chen, Y.S. Huang, H.C. Chen, Wear 261 (2006) 513–519.
[17] C.P. Lee, C.C. Chang, Y.Y. Chen, J.W. Yeh, H.C. Shih, Corrs. Sci. 50 (2008) 2053–2060.
[18] M.H. Cai, Study on the Microstructure and Electrical Properties Evolution of High-Entropy Alloy Thin Films, M.S. thesis, Department of Material Science and Engineering, NTHU, Taiwan, 2003.
[19] T. Saito, J. Alloys Compd. 505 (2009) 23–28.
[20] S. Chakraborty, A.K. Majumdar, J. Magn. Magn. Mater. 186 (1998) 357–372.
[21] A.A. Al-Aql, Mater. Des. 24 (2003) 547–550.
[22] C. Kittel, Introduction to Solid State Physics, 8th ed., Wiley, New York, 2005.
[23] P.J. Cote, L.V. Meisel, Phys. Rev. Lett. 39 (1977) 102–105.
[24] J. Kondo, Prog. Theo. Phys. 32 (1964) 37–49.
[25] B. Shen, Q. Guo, Y. Gong, W.S. Zhan, J.G. Zhao, J. Appl. Phys. 81 (1997) 4661–4663.
[26] B.D. Cullity, Introduction to Magnetic Materials, Addison-Wesley, Reading, Massachusetts, 1972.
[27] L. Berger, G. Bergmann, in: C.L. Chien, C.R. Westgate (Eds.), The Hall Effect and Its Applications, Plenum Press, New York and London, 1980.
[28] J. Smit, Physica 16 (1951) 612–627.
[29] L. Berger, Phys. Rev. B 2 (1970) 4559–4566.
[30] H. Beck, H.-J. Güntherodt (Eds.), Glassy Metals III, Topics in Applied Physics, vol. 72, Springer, Berlin, 1994.
[31] P.C. Chu, Hall effect and related electrical and magnetic properties in various quinary and senary high-entropy alloys selected from Al, Co, Cr, Fe, Ni, and Ti, M.S. thesis, Department of Material Science and Engineering, NTHU, Taiwan, 2009.